PCCP

ROYAL SOCIETY OF CHEMISTRY

PAPER

View Article Online
View Journal | View Issue

Cite this: *Phys. Chem. Chem. Phys.*, 2026, **28**, 9617

Generalizable mechanochemical impact of curvature governing stability and reactivity at catalytic sites on rippled supports

Sayan Banerjee * and Sampad Mandal

Graphene is inherently prone to forming ripples and curved regions, both with and without defects, which modify its local geometry and, consequently, its electronic structure. Such curvature effects become particularly important when graphene serves as a support for atomically dispersed single-atom catalytic sites (M–N–C), which are key motifs for small-molecule activation. These sites can be regarded as defect structures within a two-dimensional (2D) framework; however, the role of curvature as a vector descriptor—capturing both the magnitude and the direction (sign) of curvature—remains largely unexplored in reactivity analysis. Here, we investigate how the sign of curvature impacts the stability, electronic structure, and adsorption properties of M–N–C sites using first-principles density functional theory (DFT) calculations encompassing 3d, 4d, and 5d transition metal centers. We find that curvature modulates the thermodynamic stability of single-atom sites, with larger metal centers being preferentially stabilized in regions of higher curvature. Furthermore, curvature modulates key aspects of chemical bonding, including covalency and ionicity, as demonstrated using H adsorption as a model case. Curvature serves as a control parameter for tuning the M–H bonding strength, with the effect being most pronounced for early transition metals. CO_2 activation is then examined as a representative example of small-molecule activation under curvature, revealing that the nature of curvature can drastically modify the activation mechanism at a given metal center. Notably, curvature enhances CO_2 adsorption and activation even for metals that are inactive on flat surfaces. Overall, the response to curvature depends on the nature of the transition metal: early transition metals exhibit a more pronounced curvature dependence than late transition metals. This indicates that, in addition to tuning adsorption properties by changing the transition-metal site, curvature can play a non-trivial and metal-dependent role in modulating adsorption, adding an additional design dimension for active sites. Because ripples are intrinsic to 2D materials and can also be engineered through external stimuli or mechanochemical deformation, these findings demonstrate that exploiting curvature as a vector descriptor in chemical space enables new forms of reactivity inaccessible on planar surfaces.

Received 8th December 2025,
Accepted 11th March 2026

DOI: 10.1039/d5cp04759e

rsc.li/pccp

Introduction

Supported single site catalysts (SACs) on two-dimensional (2D) materials catalyze a wide range of industrially relevant reactions.[1,2] Among these, coordinationally well-defined active sites embedded within graphene supports—known as M–N–C catalysts (M: metal, N: nitrogen, and C: carbon)—have been investigated through both experimental and theoretical approaches.[2–4] M–N–C catalysts exhibit high activity toward a wide range of thermal and electrocatalytic reactions, including the oxygen reduction reaction (ORR), CO_2 reduction reaction (CO_2 RR), and other small-molecule activation processes.[2] Their remarkable performance is ascribed to the ability of atomically dispersed metal centers to host localized electronic states within an otherwise delocalized carbon framework. These sites afford molecular-level control over active-site chemistry, offering a unique lever for catalyst design.[2,5] However, their structural sensitivity renders them susceptible to perturbations that can compromise stability and performance, often leading to rapid degradation under operando conditions.[6,7]

On a different front, 2D materials inherently exhibit spontaneous rippling and curvature, encompassing both transition-metal dichalcogenides and carbon-based systems.[8–11] In particular, graphene and related graphitic materials have been shown to develop ripples even in the absence of defects.[12–17] Such out-of-plane deformations introduce nonzero curvature, leading to nontrivial effects on the electronic structure and

Department of Chemistry, University of Tennessee–Knoxville, Knoxville, TN, 37923, USA. E-mail: sbanerjee@utk.edu

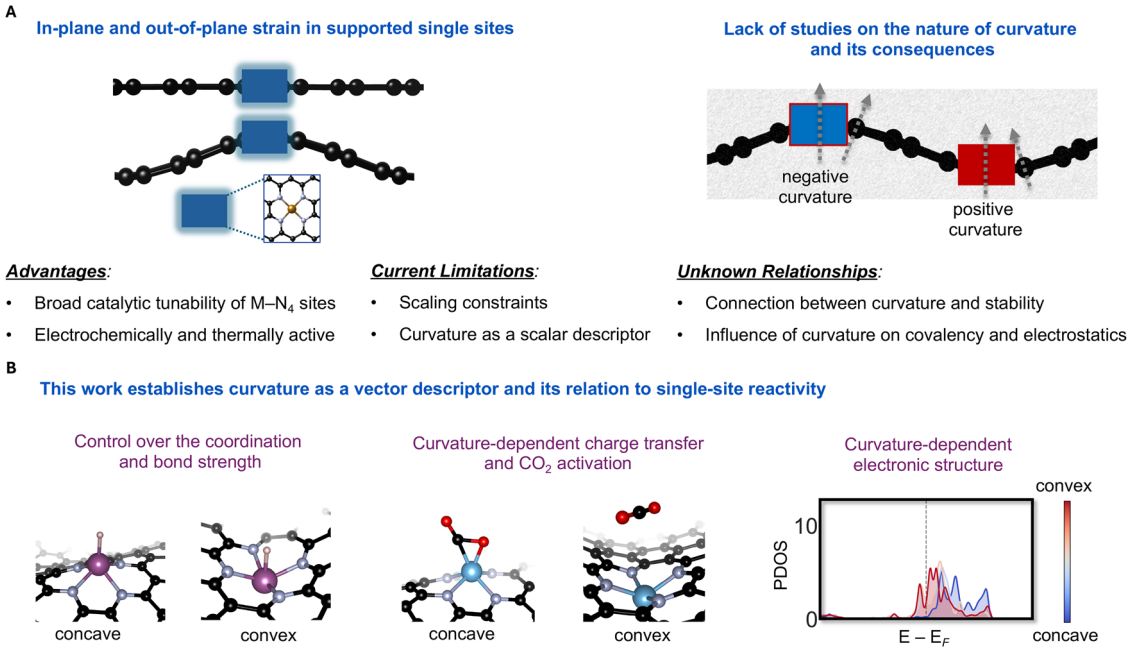

Fig. 1 (A) Summary of literature reports illustrating the effects of in-plane and out-of-plane strain on single-site M–N–C catalysts and their known limitations. The right panel emphasizes the lack of studies addressing the fundamental nature of curvature and its potential to overcome these limitations. (B) Overview of this work, showcasing how curvature introduces new design directions by modulating covalency, charge transfer, CO_2 activation, and the underlying electronic structure of single-atom active sites.

influencing phenomena ranging from optoelectronic responses to chemical reactivity.[9,18] In this context, the emerging field of rolltronics has introduced new avenues to dynamically control material curvature.[19,20] Curvature has likewise been shown to modulate surface reactivity, influencing molecular adsorption and migration on graphene.[21–23]

The active sites in SACs are often reported to be dynamic under operando conditions.[24–26] Previous studies have primarily examined the effects of in-plane and out-of-plane strain by treating curvature as a scalar descriptor (Fig. 1).[27–31] However, the role of curvature as a vector descriptor—accounting for both its magnitude and direction—has been underexplored. In particular, how local structural perturbations in SACs embedded within 2D matrices at regions of differing curvature (*i.e.*, negatively curved concave and positively curved convex sites) influence the electronic structure and catalytic properties remains unknown (Fig. 1). Because ripples inherently generate regions with distinct curvature types, systematic investigation is essential to elucidate the atomistic mechanisms of SACs under curvature and to predict new avenues of curvature-driven reactivity.

To elucidate how spontaneous ripples in 2D materials affect the stability and catalytic behavior of M–N–C sites—and to establish a predictive framework for exploiting curvature in tuning SAC performance—we investigate the influence of curvature on the stability and electronic structure of SACs with transition metal (TM) centers spanning the 3d, 4d, and 5d series (Fig. 1). Hydrogen adsorption is examined as a model case to probe how curvature modulates the fundamental nature of chemical bonding, while CO_2 activation is explored to reveal how curvature can be harnessed to induce new reactivity and small-molecule activation mechanisms. Specifically, we study MN_4 active sites for M–N–C SACs supported on a sinusoidally curved graphene matrix, employed here as a model system to quantify curvature effects.

We first examine the relationship between curvature and the formation energy of single sites and find that TMs with larger metallic radii are preferentially stabilized in regions of high curvature. The relative stability correlates strongly with local geometric descriptors, indicating that the observed stability originates primarily from geometric effects. On the adsorption properties front, the H binding energy increases with negative (concave) curvature for all TMs, indicating universally stronger binding in concave regions. We further show that curvature fundamentally alters the nature of chemical bonding, providing a new handle to control both covalency and ionicity as a function of geometric deformation. We then extend this framework to CO_2 activation as a representative case of small-molecule activation under curvature. The nature of curvature is found to drastically modify the activation mechanism at a given metal center. Notably, curvature can enhance CO_2 adsorption and activation even for TMs that are inactive on flat surfaces. Across the TM series, we find a metal-specific curvature response that highlights a clear metal–curvature interplay: early TMs consistently show a stronger response to curvature than late TMs. Curvature-dependent charge transfer and variable binding modes are observed, underscoring the interplay between local geometry and electronic structure. Overall, our findings establish curvature as a critical design parameter for controlling reactivity at single-atom sites by directly tuning their local geometric and electronic environments.

Results and discussion

Effect of curvature on stability of single sites

Formation energies (E_f) of TM single sites in M–N–C catalysts with MN_4 coordination were calculated for 3d, 4d, and 5d elements supported on a curved graphene surface (curvature = 0.12 $Å^{-1}$) (Fig. 2A). The objective is to determine how curvature influences the stability of SACs across the TM series. While the absolute E_f depends on the magnitude of curvature, here we focus on trends across metals at a fixed curvature. In Fig. 2A, the formation energies (E_f) at a curvature of 0.12 $Å^{-1}$ are presented as a representative case.

A more negative E_f indicates that site formation on the curved surface is energetically more favorable, while a more positive value corresponds to a lower tendency for site formation under curvature. For MN_4 sites, the variation in E_f follows the trend in metallic radii. Within the 3d series, Sc and Ti favor curved surfaces, whereas mid- and late-series TMs show lower stability under curvature. Zn again becomes stabilized after Cu, consistent with the size-dependent trend. A similar pattern is observed for the 4d series, although the magnitude of stabilization is smaller, consistent with the generally weaker metal–nitrogen interaction for 4d elements. The same qualitative behavior extends to the 5d series, again correlating with atomic size. Across all three rows, the 3d elements show more negative formation energies than their 4d and 5d analogues, consistent with stronger M–N bonding. This trend persists down each TM group in the periodic table.

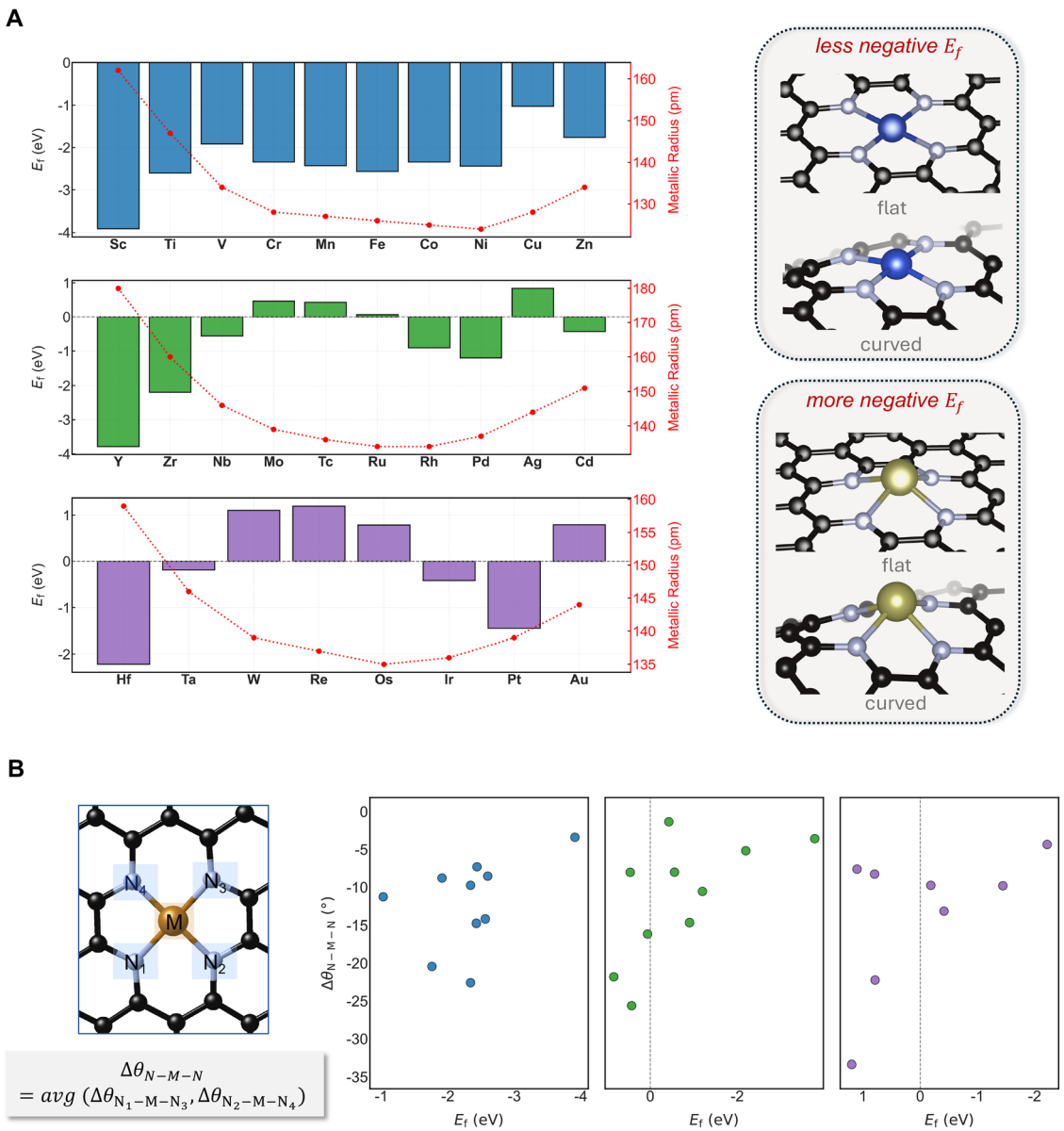

Fig. 2 Formation energies of MN_4 sites. (A) Formation energy (E_f) is plotted, where a more negative value indicates higher stability at curved sites. The metallic radius is shown as an additional axis for reference. The right panel shows representative cases illustrating preferred configurations: Cu and Hf correspond to less and more negative E_f, respectively. (B) Plot of the change in N–M–N bond angle ($\Delta\theta_{N-M-N}$) between flat and curved supports *versus* E_f for 3d, 4d, and 5d TMs. A lower deviation in $\Delta\theta_{N-M-N}$ correlates with higher stability at curved sites. The curved structures are modeled at a curvature of 0.12 $Å^{-1}$.

To examine the origin of the E_f trends under curvature, the computed E_f values were correlated with the relative change in the diagonal N–M–N bond angle ($\Delta\theta_{N-M-N}$) between flat and curved surfaces across the 3d, 4d, and 5d series (Fig. 2B). A larger $\Delta\theta_{N-M-N}$—indicating greater structural reorganization at the active site under curvature—correlates with reduced stabilization on curved surfaces. For TMs on flat supports, late elements exhibit nearly linear N–M–N angles (close to 180°), whereas early TMs show greater deviation from linearity, consistent with their larger metallic radii. Curved surfaces can accommodate and promote such distortions, leading to stabilization for larger metal centers, as reflected in smaller $\Delta\theta_{N-M-N}$ values for more negative E_f. In contrast, metals that exhibit minimal distortion on flat supports, typically smaller-radius TMs, show limited stabilization under curvature since the required geometric distortion is larger (higher $\Delta\theta_{N-M-N}$), resulting in destabilization. Overall, the geometric descriptor $\Delta\theta_{N-M-N}$ captures how curvature affects TM stability differently for early and late TMs, originating from the structural preference of larger-radius metals for more distorted active sites.

Curvature-dependent H binding across transition metals

H binding energies (ΔE_H) were calculated at four distinct curvature values (0.12, 0.02, −0.02, and −0.12 Å^{-1}), encompassing both high and low magnitudes of positive and negative curvature, for 3d, 4d, and 5d TMs (Fig. 3A). The presence of an adsorbate breaks the inherent symmetry between concave and convex regions, providing a basis to treat curvature as a vector quantity. This formulation enables examination of how both the nature (sign) and magnitude of curvature influence H adsorption, thereby establishing a model framework for understanding chemisorption as a function of curvature.

In all cases where substantial variation in adsorption energy is observed, H adsorption is stronger at negatively curved (concave) sites than at positively curved (convex) sites. This trend holds across the 3d, 4d, and 5d series, although the magnitude of ΔE_H varies from one TM to another. Early TMs in each series exhibit a pronounced curvature dependence, as evidenced by the large difference in ΔE_H between the highest positive and negative curvature values considered (Fig. 3A). The sensitivity of ΔE_H to curvature decreases systematically toward the late TMs. Notably, Cd and Au deviate from these general trends, displaying stronger curvature dependence than expected. This deviation arises from their preference for MN_3-type coordination, which distinguishes their behavior from that of the other metals studied.[32–34] Since MN_3-type sites are not considered in this work, Cd and Au are excluded from further analysis. However, it is noteworthy that both Cd and Au exhibit stronger H binding at negatively curved regions compared to their positively curved counterparts.

For early TMs, H adsorption at concave and convex sites results in markedly different local geometries. At concave sites,

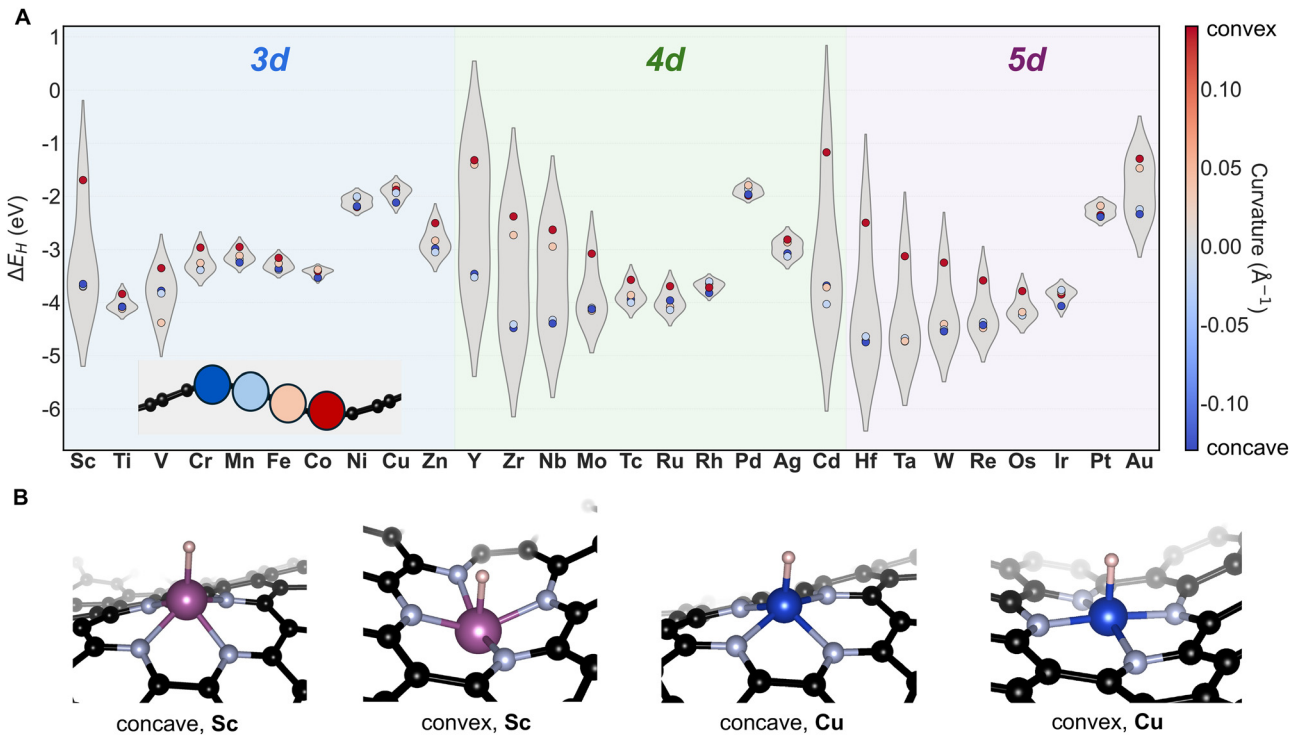

Fig. 3 Curvature-dependent H binding energy. (A) Violin plots of H binding energy (ΔE_H) as a function of curvature for all transition metals. The curvature values are color coded, and their corresponding positions are shown in the inset. The presence of adsorbed H breaks the symmetry between concave and convex sites. (B) Representative binding geometries for elements exhibiting high and low curvature dependence in ΔE_H. Sc is shown as an example of strong curvature sensitivity, while Cu represents a case with minimal variation. Geometries are shown for curvatures of ±0.12 Å^{-1}. Color code: C (black), N (light blue), Cu (blue), and Sc (purple).

a square-pyramidal configuration is favored due to the geometric tendency of these regions toward pyramidalization (Fig. 3B). The larger atomic radii of early TMs, combined with their propensity to pucker the M–N–C framework, lead to enhanced stabilization at concave sites. Such puckering cannot be easily accommodated at convex sites, where the structure instead adopts an inverse bowl-like geometry, resulting in lower stability. Late TMs, which display minimal variation in ΔE_H, show less puckering at the active site as a function of curvature, consistent with their lower affinity for curved surfaces (Fig. 2). Moreover, at convex sites, the degree of puckering is significantly reduced for late TMs (Fig. 3B), yielding relatively flat geometries and consequently smaller variations in ΔE_H.

To assess whether curvature-dependent H binding could be influenced by steric (secondary-sphere-like) interactions imposed by the local geometry—differently at concave *versus* convex sites—we carried out two complementary analyses. We selected three metals: Sc, which exhibits a stronger curvature dependence in H binding, and Fe and Cu, which exhibit relatively weaker curvature dependence. First, we introduced an additional concave layer to quantify the repulsive contribution experienced by the adsorbed H at the convex face and found that, while a repulsive term is present, it is largely interlayer in origin and does not track the metal-dependent H binding-energy trend. Second, we mapped the H potential energy surface for displacements (i) toward nearby C/N groups and (ii) along the M–H bond coordinate. Differences have been observed between the concave and convex cases; however, the magnitude is too small to account for the binding-energy differences between convex and concave faces. In contrast, the dominant curvature-dependent changes emerge along the M–H bond coordinate, consistent with curvature primarily modulating intrinsic metal–adsorbate bonding rather than steric repulsion from the surrounding framework. Full computational details and PES scans are provided in the SI (Fig. S9 and S10).

It is worth noting that the H binding energy varies with transition-metal identity, highlighting the role of elemental identity in setting the baseline H affinity. Beyond this, within each transition metal the remaining spread reflects the impact of curvature on the binding energy. Importantly, the magnitude

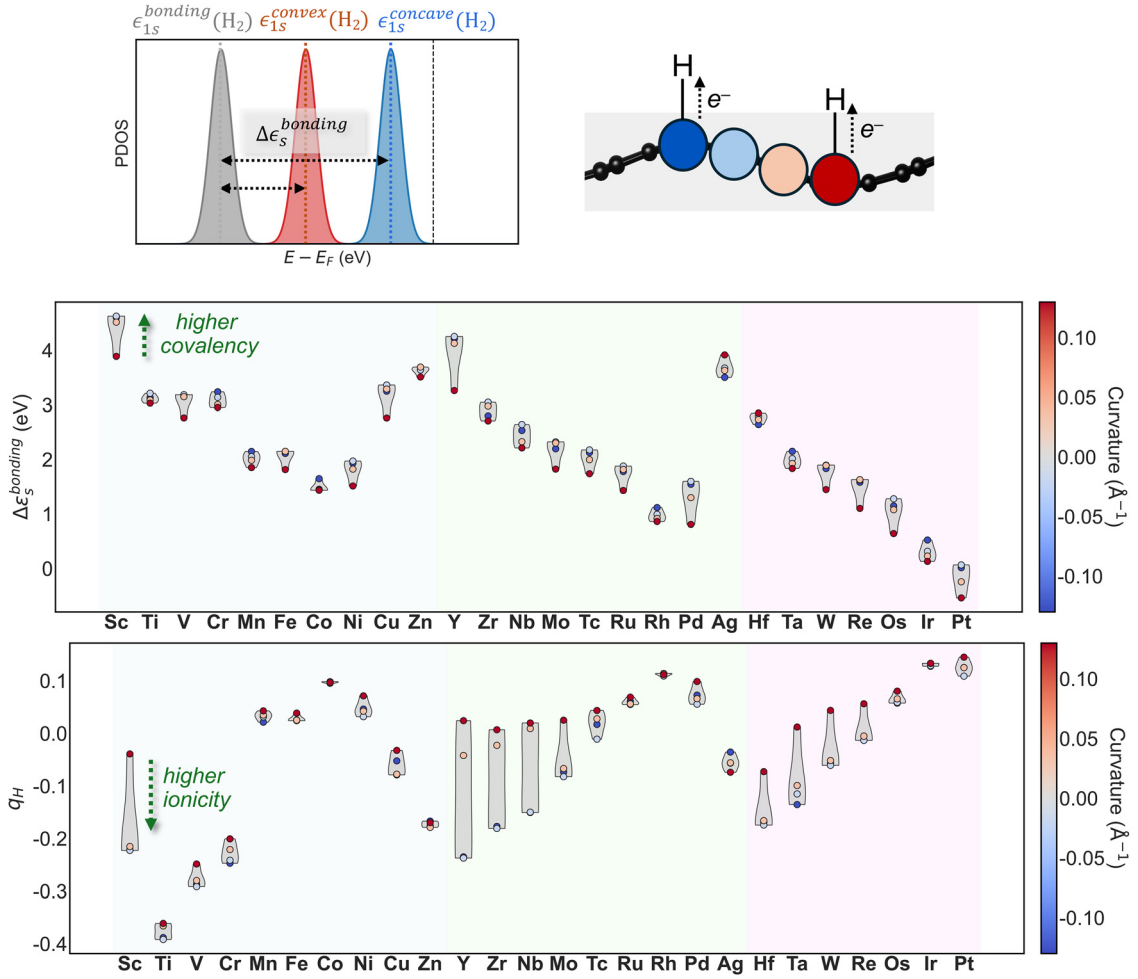

Fig. 4 Origin of curvature-dependent H binding energy. The extent of covalency is defined as $\Delta\varepsilon_{1s}^{bonding}$, which represents the difference between the band center of adsorbed H and that of isolated H_2 ($\varepsilon_{1s}^{bonding}$). Ionicity is quantified using the Löwdin charge of the adsorbed H atom. The middle panel shows $\Delta\varepsilon_{1s}^{bonding}$ for different metals, while the lower panel depicts the Löwdin charge of H in the adsorbed geometry.

of this curvature-driven variation depends on the metal, leading to a metal-specific curvature response and underscoring that curvature can be exploited as a design handle in a manner that depends on the nature of the TM. Overall, these results demonstrate that the nature of curvature fundamentally modulates H binding, with chemisorption generally becoming stronger at negatively curved (concave) sites.

Covalency and ionicity as a function of curvature

We investigate the origin of the ΔE_H trends, specifically how curvature modulates key aspects of chemical bonding—namely, the covalency and ionicity of the M–H bond (Fig. 4). To this end, we calculated the projected density of states (PDOS) and Löwdin charges. The extent of covalency is defined as $\Delta\varepsilon_{1s}^{bonding}$ (see Methods section and the SI), which represents the difference between the band center of adsorbed H and that of isolated H_2 ($\varepsilon_{1s}^{bonding}$) (Fig. 4). The 1s band center of H_2 is evaluated by placing the molecule within the simulation box of the curved slab, but 10 Å away from the surface along the *z*-axis, enabling direct alignment and comparison with the 1s band of H in the M–H bond. This approach provides a consistent framework to compare the band center shifts across different metals. A larger value of $\Delta\varepsilon_{1s}^{bonding}$ indicates a stronger covalent interaction, as a greater shift relative to the H_2 reference reflects enhanced orbital mixing.[35–37] Concave regions consistently exhibit higher $\Delta\varepsilon_{1s}^{bonding}$ values, corresponding to stronger M–H interactions compared to convex regions (blue *vs.* red dots in the middle panel of Fig. 4). Furthermore, early TMs display larger shifts than late TMs, consistent with their stronger H binding across curvature regions (Fig. 4). This universal trend of enhanced covalency at negatively curved (concave) sites demonstrates that curvature introduces a fundamentally new design parameter whose qualitative effect is largely independent of the metal identity.

Next, we evaluate the ionicity, quantified by how hydridic the H atom is in the M–H bond. Similar to the covalency trend, ionicity also exhibits a universal curvature dependence (Fig. 4), as evidenced by the more hydridic nature of H at concave regions. We find that H atoms bound at concave (negatively curved) sites display greater hydridic character compared to those at convex sites. Early TMs show both a higher degree of ionicity and a larger variation across curvature values than late TMs, reflecting their stronger electrostatic interactions. Consequently, curvature modulates electrostatic effects in a metal-dependent fashion, with early TMs being more susceptible to curvature-induced charge transfer. Overall, these findings demonstrate that curvature can systematically tune both covalency and ionicity, offering a general route to manipulate fundamental aspects of chemical bonding through curvature.

Curvature-dependent CO_2 binding and charge transfer

To demonstrate that curvature can be exploited to facilitate small-molecule chemistry, we investigated CO_2 activation as a function of curvature (Fig. 5). This analysis is motivated by the well-established role of local electrostatics and the surrounding chemical environment in governing CO_2 activation.[38–42]

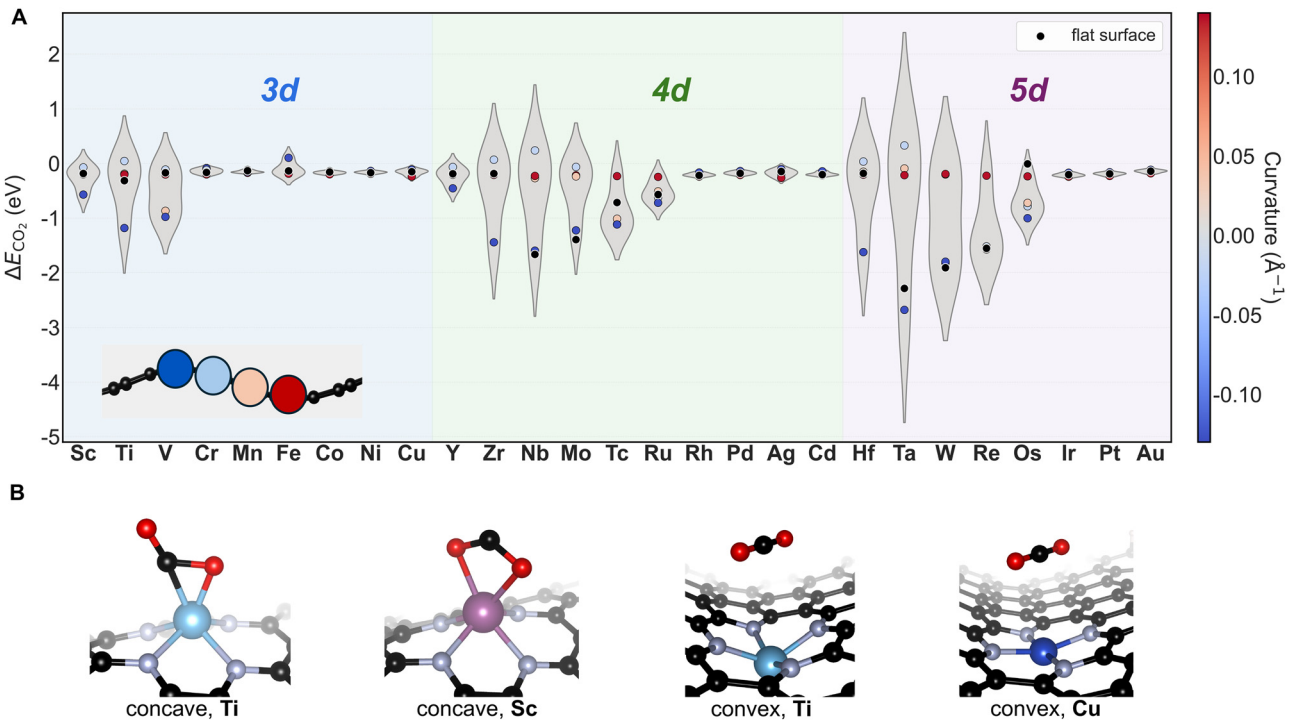

Fig. 5 Curvature-dependent CO_2 binding energy. (A) CO_2 binding energy (ΔE_{CO_2}) plotted as a function of curvature for 3d, 4d, and 5d transition metals. A larger variation is observed for early transition metals compared to late transition metals. The inset shows the regions where CO_2 binding was evaluated. (B) Representative binding motifs as a function of curvature.

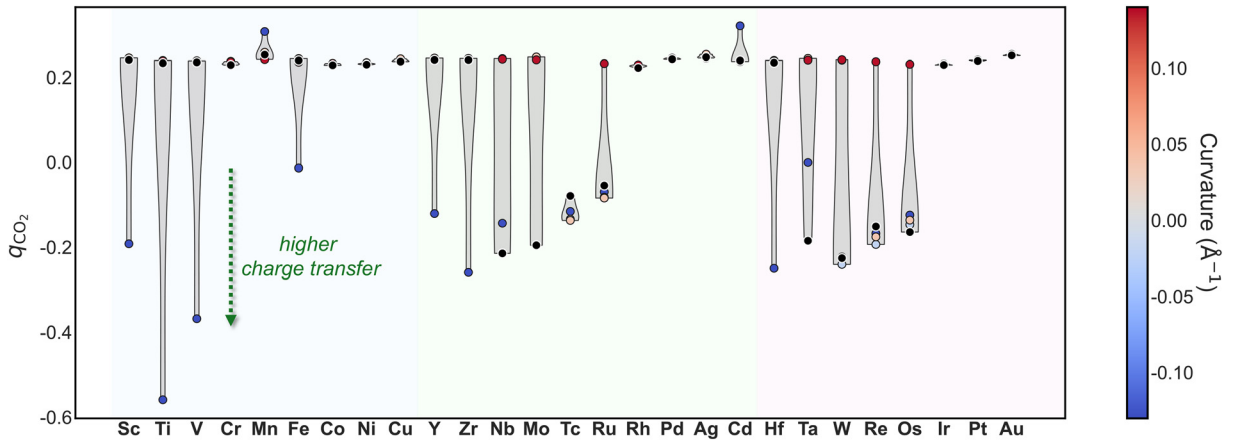

Fig. 6 Curvature-dependent charge transfer associated with CO_2 activation on curved surfaces across the metal series.

As shown earlier, curvature can fundamentally modulate electrostatics and covalency; here, we explore how variations in these factors can be leveraged to promote facile CO_2 activation.

For CO_2 binding (ΔE_{CO_2}), we find that early TMs exhibit a strong dependence on the nature of curvature (Fig. 5A). Specifically, curvature-dependent activation mechanisms are observed: at negatively curved (concave) sites, early TMs bind CO_2 more strongly through metal–CO_2 bond formation, whereas at positively curved (convex) regions, the same metals do not activate CO_2 and only weak noncovalent interactions are present. In other words, the nature of curvature can fundamentally switch the adsorption process between chemisorption and physisorption at the same metal center. This behavior arises because convex structures restrict CO_2 binding due to geometric puckering of the M–N–C framework, which limits orbital overlap at the convex face (Fig. 5B). Depending on both the nature of curvature and the identity of the TM, variable CO_2 adsorption modes are observed. For large-radius TMs such as Ti and Hf, η_2-type binding through a C–O bond accompanied by C–O bond activation is observed (Fig. 5B). Additionally, for Sc, we identify a κ_2-type CO_2 binding mode involving both O atoms, consistent with coordination motifs previously reported in organometallic chemistry.[41,43] In contrast, late TMs show negligible CO_2 activation, even on curved surfaces. Moreover, CO_2 activation is not observed at low curvature magnitudes for any TM; it emerges only at higher curvature values. At low curvature, early TM sites undergo significant structural distortion, preventing CO_2 from binding effectively and resulting instead in weak physisorption.

The number of metals exhibiting significant curvature dependence increases from the 3d to the 5d series—specifically, Sc, Ti, and V among the 3d metals; Y, Zr, Nb, Mo, and Tc among the 4d; and Hf, Ta, W, Re, and Os among the 5d (Fig. 5A). This systematic behavior highlights the critical role of atomic size in determining curvature-induced activation. Notably, several TMs that do not activate CO_2 on flat supports (*e.g.*, Sc, Ti, V, Y, Zr, Hf, and Os) can activate CO_2 on curved surfaces. We further quantify the extent of charge transfer at different curvatures by computing the Löwdin charge on CO_2 in the bound geometry (Fig. 6). Appreciable curvature-dependent charge transfer is observed for early TMs, with enhanced charge transfer at negatively curved (concave) regions, whereas late TMs show little variation. As shown in Fig. 5 and 6, the degree of charge transfer strongly correlates with the extent of CO_2 activation. Overall, metals exhibiting stronger electrostatic interactions demonstrate a higher sensitivity of charge transfer to curvature. These results establish that curvature-dependent charge transfer from curved surfaces to small molecules such as CO_2 can be harnessed to enable facile activation.

These findings demonstrate that curvature can fundamentally alter the CO_2 activation mechanism at a single atom metal site. This reveals new design principles in which curvature can be exploited to tune local bonding environments and enable novel mechanistic pathways for CO_2 activation. Conversely, in most cases, weaker CO_2 binding is observed at positively curved (convex) regions, suggesting that such motifs are less promising for catalyst design. That said, the influence of curvature on the solvation structure near the active site and the associated dynamics under an external bias are not addressed here. These effects could be non-trivial and may introduce additional design principles for harnessing curvature under realistic catalytic conditions, including electrocatalytic CO_2 reduction.

Overall, these results indicate that catalytic performance on 2D supports—particularly for adsorbates such as H and CO_2 can carry an inherent curvature dependence and/or be engineered through deliberate curvature control. This further suggests that catalytic responses on corrugated surfaces should account for multiple curvature motifs to predict performance under realistic, dynamic conditions. In this context, synthesis and dynamic mechanochemical effects can play critical roles: static curvature may be introduced *via* strain-engineered synthesis,[18] while dynamic curvature could, for example, be induced by mechanical perturbations such as AFM-tip dragging.[44,45] To quantify such effects experimentally, combining operando electrochemical measurements with spatially resolved microscopy offers a route to correlate spatially varying curvature with adsorption properties.

However, it is worth noting that the present work models a simplified, sinusoidal curvature motif. In contrast, realistic

surfaces can exhibit a heterogeneous combination of curvature features (*e.g.*, ripples, domes, and bubbles) and corresponding catalytic motifs. Capturing such complexity will ultimately require an ensemble-averaged description over possible curvature motifs to predict performance at spatially extended scales, motivating future methodological development. The current study provides a foundation by demonstrating that curvature can influence the electronic structure and associated properties in a non-trivial manner, thereby offering an underexplored design dimension to exploit.

Conclusions

Overall, we demonstrate that curvature, treated as a vector quantity, provides an underexplored design dimension for tuning the stability, electronic structure, and reactivity of single-atom M–N–C catalysts. Through systematic analysis across the 3d, 4d, and 5d transition metal series, we show that curvature fundamentally alters the local bonding environment and, consequently, the thermodynamics of site formation and adsorption. Moreover, we demonstrate that the nature of the TM dictates the curvature response, thereby providing a clear avenue to harness curvature in a targeted manner for specific classes of active sites. Negatively curved (concave) regions act as active pockets that stabilize larger metal centers, strengthen H adsorption, and facilitate CO_2 activation, whereas positively curved (convex) regions suppress chemisorption. These effects arise from curvature-induced modifications in both geometric distortion and electronic structure, which together control the interplay between covalency and ionicity at the active site. By simultaneously tuning the covalent and ionic character of metal–adsorbate interactions, curvature enables distinct mechanisms of small-molecule activation that are not accessible on flat surfaces. From a broader perspective, engineering curvature through approaches such as mechanochemical deformation, strain patterning, or substrate-induced rippling can open new directions in catalyst design. Such strategies offer opportunities to access reactivity regimes that are traditionally unattainable through chemical substitution or planar strain engineering.

Methods

All density functional theory (DFT) calculations were performed using the Quantum Espresso software package.[46] The generalized gradient approximation (GGA) with the Perdew–Burke–Ernzerhof (PBE) exchange–correlation functional was employed.[47] Ultrasoft GBRV pseudopotentials were used with kinetic-energy and charge-density cutoffs of 35 Ry and 350 Ry, respectively.[48] Dispersion interactions were included *via* the DFT-D3 correction developed by Grimme and co-workers.[49] All structures were fully relaxed until the forces on each atom were below 1.0×10^{-3} a.u., and the total-energy convergence criterion was set to 1.0×10^{-4} a.u. A (6×6) graphene supercell was used to investigate the effect of curvature on adsorption and migration behavior. A vacuum spacing of approximately 20 Å was introduced along the surface normal to eliminate spurious periodic interactions. A Γ-centered $(2 \times 2 \times 1)$ Monkhorst–Pack grid was used to sample the Brillouin zone.[50] To ensure consistent rumpling amplitude and sinusoidal curvature profiles, a single hydrogen atom was placed near the crest (mountain) region in all simulations. The use of one H adsorbate per supercell preserves the intrinsic curvature and minimizes artificial electronic effects; this approach has been validated previously, and our results confirm its qualitative consistency.[22] Further computational details are provided in the SI. The adsorption (binding) energies of H and CO_2 were computed as

$$\Delta E_{\mathrm{H}} = E_{\mathrm{H}^*} - E_{\mathrm{bare}} - E_{\mathrm{H}}, \quad (1)$$

$$\Delta E_{\mathrm{CO_2}} = E_{\mathrm{CO_2}^*} - E_{\mathrm{bare}} - E_{\mathrm{CO_2}}, \quad (2)$$

where E_{H^*} and $E_{\mathrm{CO_2}^*}$ correspond to the total electronic energies of the adsorbed systems, and E_{bare}, E_{H}, and $E_{\mathrm{CO_2}}$ denote the total electronic energies of the clean slab, gas-phase H atom, and isolated CO_2 molecule, respectively. Formation energies (E_{f}) were calculated relative to the bulk metal reference (E_{M}) as

$$E_{\mathrm{f}} = E_{\mathrm{slab+M}} - E_{\mathrm{slab}} - E_{\mathrm{M}}. \quad (3)$$

$$\varepsilon_{\mathrm{s}}^{\mathrm{bond}} = \frac{\int_{E_{\mathrm{min}}}^{E_{\mathrm{F}}} E D_{\mathrm{s}}(E)\mathrm{d}E}{\int_{E_{\mathrm{min}}}^{E_{\mathrm{F}}} D_{\mathrm{s}}(E)\mathrm{d}E}. \quad (4)$$

The bonding s-band center is defined as $\varepsilon_{\mathrm{s}}^{\mathrm{bond}}$, where $D_{\mathrm{s}}(E)$ is the s-projected density of states (PDOS), and E_{min} denotes the lower integration limit, chosen sufficiently below the valence manifold (typically $E_{\mathrm{min}} = -15$ eV with respect to the Fermi level). The denominator normalizes the PDOS weight below E_{F}, while the numerator yields the first moment of the occupied s-state distribution. To enable a consistent reference of the calculated $\varepsilon_{\mathrm{s}}^{\mathrm{bond}}$ values across different systems, the descriptor is referenced to the 1s band center of a gas-phase H_2 molecule placed in the same simulation cell. The relative bonding s-level shift is therefore expressed as

$$\Delta\varepsilon_{\mathrm{s}}^{\mathrm{bond}} = \varepsilon_{1\mathrm{s}}^{\mathrm{bond}}(\mathrm{M–H}) - \varepsilon_{1\mathrm{s}}^{\mathrm{bond}}(\mathrm{H–H}), \quad (5)$$

where $\varepsilon_{1\mathrm{s}}^{\mathrm{bond}}$(M–H) and $\varepsilon_{1\mathrm{s}}^{\mathrm{bond}}$(H–H) denote the 1s-derived bonding levels of the surface-bound H atom and H of the H_2 molecule.

Conflicts of interest

The authors declare no competing financial interest.

Data availability

All calculation details required to evaluate the conclusions of this study are available in the supplementary information (SI). Supplementary information: additional density functional theory (DFT) calculation details and electronic structure analyses. See DOI: https://doi.org/10.1039/d5cp04759e.

Structural coordinates used in the calculations are available in the Banerjee Group GitHub repository (https://github.com/banerjee-group-utk/PCCP-2026-D5CP04759E).

Acknowledgements

This work was supported by startup funds from the University of Tennessee, Knoxville. This research used resources of the National Energy Research Scientific Computing Center, a DOE Office of Science User Facility supported by the Office of Science of the U.S. Department of Energy under Contract No. DE-AC02-05CH11231 using NERSC award NERSC DDR-ERCAP0035235.

References

1 L. Liu and A. Corma, Metal Catalysts for Heterogeneous Catalysis: From Single Atoms to Nanoclusters and Nanoparticles, *Chem. Rev.*, 2018, **118**, 4981–5079.
2 H.-Y. Zhuo, X. Zhang, J.-X. Liang, Q. Yu, H. Xiao and J. Li, Theoretical Understandings of Graphene-based Metal Single-Atom Catalysts: Stability and Catalytic Performance, *Chem. Rev.*, 2020, **120**, 12315–12341.
3 H. Fei, *et al.*, General synthesis and definitive structural identification of MN_4C_4 singleatom catalysts with tunable electrocatalytic activities, *Nat. Catal.*, 2018, **1**, 63–72.
4 S. Kment, A. Bakandritsos, I. Tantis, H. Kmentova, Y. Zuo, O. Henrotte, A. Naldoni, M. Otyepka, R. S. Varma and R. Zboril, Single Atom Catalysts Based on Earth-Abundant Metals for Energy-Related Applications, *Chem. Rev.*, 2024, **124**, 11767–11847.
5 J. S. Bates, M. R. Johnson, F. Khamespanah, T. W. Root and S. S. Stahl, Heterogeneous M-N-C Catalysts for Aerobic Oxidation Reactions: Lessons from Oxygen Reduction Electrocatalysts: Focus Review, *Chem. Rev.*, 2022, **123**, 6233–6256.
6 K. L. Branch, E. R. Johnson and E. M. Nichols, Porphyrin Aggregation under Homogeneous Conditions Inhibits Electrocatalysis: A Case Study on CO_2 Reduction, *ACS Cent. Sci.*, 2024, **10**, 1251–1261.
7 K. Kumar, L. Dubau, F. Jaouen and F. Maillard, Review on the Degradation Mechanisms of Metal-N-C Catalysts for the Oxygen Reduction Reaction in Acid Electrolyte: Current Understanding and Mitigation Approaches, *Chem. Rev.*, 2023, **123**, 9265–9326.
8 F. L. Thiemann, C. Scalliet, E. A. Müller and A. Michaelides, Defects induce phase transition from dynamic to static rippling in graphene, *Proc. Natl. Acad. Sci. U. S. A.*, 2025, 122.
9 T. P. Darlington, *et al.*, Imaging strain-localized excitons in nanoscale bubbles of monolayer WSe_2 at room temperature, *Nat. Nanotechnol.*, 2020, **15**, 854–860.
10 D. Lloyd, X. Liu, J. W. Christopher, L. Cantley, A. Wadehra, B. L. Kim, B. B. Goldberg, A. K. Swan and J. S. Bunch, Band Gap Engineering with Ultralarge Biaxial Strains in Suspended Monolayer MoS_2, *Nano Lett.*, 2016, **16**, 5836–5841.
11 Y. Gao, F. Deng, R. He and Z. Zhong, Spontaneous curvature in two-dimensional van der Waals heterostructures, *Nat. Commun.*, 2025, **16**, 717.
12 M. Ackerman, P. Kumar, M. Neek-Amal, P. Thibado, F. Peeters and S. Singh, Anomalous Dynamical Behavior of Freestanding Graphene Membranes, *Phys. Rev. Lett.*, 2016, **117**, 126801.
13 J. K. Schoelz, P. Xu, V. Meunier, P. Kumar, M. Neek-Amal, P. M. Thibado and F. M. Peeters, Graphene ripples as a realization of a two-dimensional Ising model: A scanning tunneling microscope study, *Phys. Rev. B: Condens. Matter Mater. Phys.*, 2015, **91**, 045413.
14 M. Neek-Amal, P. Xu, J. Schoelz, M. Ackerman, S. Barber, P. Thibado, A. Sadeghi and F. Peeters, Thermal mirror buckling in freestanding graphene locally controlled by scanning tunnelling microscopy, *Nat. Commun.*, 2014, **5**, 4962.
15 S. Deng, D. Rhee, W.-K. Lee, S. Che, B. Keisham, V. Berry and T. W. Odom, Graphene Wrinkles Enable Spatially Defined Chemistry, *Nano Lett.*, 2019, **19**, 5640–5646.
16 Y. Shen, E. Dai, X. Liu, W. Pan, H. Yang, B. Xiong and D. Zerulla, Curvature analysis of single layer graphene on the basis of extreme low-frequency Raman spectroscopy, *Appl. Phys. Lett.*, 2019, **114**, 161907.
17 Y. Zhang, T. Gao, Y. Gao, S. Xie, Q. Ji, K. Yan, H. Peng and Z. Liu, Defect-like Structures of Graphene on Copper Foils for Strain Relief Investigated by High-Resolution Scanning Tunneling Microscopy, *ACS Nano*, 2011, **5**, 4014–4022.
18 N. Hawthorne, S. Banerjee, Q. Moore, A. M. Rappe and J. D. Batteas, Studies of the Reactivity of Graphene Driven by Mechanical Distortions, *J. Phys. Chem. C*, 2022, **126**, 17569–17578.
19 B. Zhao, *et al.*, High-order superlattices by rolling up van der Waals heterostructures, *Nature*, 2021, **591**, 385–390.
20 E. Zhang, *et al.*, Graphene rolls with tunable chirality, *Nat. Mater.*, 2025, **24**, 377–383.
21 S. Banerjee, N. Hawthorne, J. D. Batteas and A. M. Rappe, Two-Legged Molecular Walker and Curvature: Mechanochemical Ring Migration on Graphene, *J. Am. Chem. Soc.*, 2023, **145**, 26765–26773.
22 S. Banerjee and A. M. Rappe, Mechanochemical Molecular Migration on Graphene, *J. Am. Chem. Soc.*, 2022, **144**, 7181–7188.
23 S. Banerjee and A. M. Rappe, Mechanochemical Molecular Motion Using Noncovalent Interactions on Graphene and Its Application to Tailoring the Adsorption Energetics. ACS, *Mater. Lett.*, 2023, **5**, 574–579.
24 Y. Han, Y. Wei, A. Goswami and A. Alexandrova, Uncovering the True Active Sites in Ni–N–C Catalysts for CO_2 Electroreduction, *J. Am. Chem. Soc.*, 2025, **147**, 38636–38646.
25 Z. Levell, S. Yu, R. Wang and Y. Liu, What Is the ''Other'' Site in M–N–C?, *J. Am. Chem. Soc.*, 2024, **147**, 603–609.
26 D. Gao, T. Liu, G. Wang and X. Bao, Structure Sensitivity in Single-Atom Catalysis toward CO_2 Electroreduction, *ACS Energy Lett.*, 2021, **6**, 713–727.
27 J. Su, *et al.*, Strain enhances the activity of molecular electrocatalysts *via* carbon nanotube supports, *Nat. Catal.*, 2023, **6**, 818–828.
28 Y. Wang, Z. Bao, M. Shi, Z. Liang, R. Cao and H. Zheng, The Role of Surface Curvature in Electrocatalysts, *Chem. – Eur. J.*, 2022, **28**, e202102915.

29 C. Liu, Q. Chen, Z. Chen, J. Wang, H. Wang, L. Luo, X. Li, Q. Jiang, T. Zheng and C. Xia, Substrate Curvature Enhances Molecular Electrocatalysts for the Efficient Production of Hydrogen Peroxide, *Nano Lett.*, 2025, **25**, 16013–16019.
30 M. Weh, A. A. Kroeger, O. Anhalt, A. Karton and F. Würthner, Mutual induced fit transition structure stabilization of corannulene's bowl-to-bowl inversion in a perylene bisimide cyclophane, *Chem. Sci.*, 2024, **15**, 609–617.
31 R. Cepitis, N. Kongi, J. Rossmeisl and V. Ivaništšev, Surface Curvature Effect on Dual-Atom Site Oxygen Electrocatalysis, *ACS Energy Lett.*, 2023, **8**, 1330–1335.
32 J. Feng, H. Gao, L. Zheng, Z. Chen, S. Zeng, C. Jiang, H. Dong, L. Liu, S. Zhang and X. Zhang, A Mn-N3 single-atom catalyst embedded in graphitic carbon nitride for efficient CO_2 electroreduction, *Nat. Commun.*, 2020, 11.
33 Q. Pan, Y. Chen, S. Jiang, X. Cui, G. Ma and T. Ma, Insight into the active sites of M–N–C single-atom catalysts for electrochemical CO_2 reduction, *Energy Chem.*, 2023, **5**, 100114.
34 J. Song, N. Hou, X. Liu, M. Antonietti, Y. Wang and Y. Mu, Unsaturated single-atom CoN_3 sites for improved Fenton-like reaction towards high-valent metal species, *Appl. Catal., B*, 2023, **325**, 122368.
35 T. D. Spivey and A. Holewinski, Selective Interactions between Free-Atom-like d-States in Single-Atom Alloy Catalysts and Near-Frontier Molecular Orbitals, *J. Am. Chem. Soc.*, 2021, **143**, 11897–11902.
36 S. Banerjee, A. Kakekhani, R. B. Wexler and A. M. Rappe, Relationship between the Surface Reconstruction of Nickel Phosphides and Their Activity toward the Hydrogen Evolution Reaction, *ACS Catal.*, 2023, **13**, 4611–4621.
37 M. T. Greiner, T. E. Jones, S. Beeg, L. Zwiener, M. Scherzer, F. Girgsdies, S. Piccinin, M. Armbrüster, A. Knop-Gericke and R. Schlögl, Free-atom-like d states in single-atom alloy catalysts, *Nat. Chem.*, 2018, **10**, 1008–1015.
38 G. O. Kayode, A. F. Hill and M. M. Montemore, Bayesian optimization of single-atom alloys and other bimetallics: efficient screening for alkane transformations, CO_2 reduction, and hydrogen evolution, *J. Mater. Chem. A*, 2023, **11**, 19128–19137.
39 D. Behrendt, S. Banerjee, C. Clark and A. M. Rappe, High-Throughput Computational Screening of Bioinspired Dual-Atom Alloys for CO_2 Activation, *J. Am. Chem. Soc.*, 2023, **145**, 4730–4735.
40 N. W. Kinzel, C. Werlé and W. Leitner, Transition Metal Complexes as Catalysts for the Electroconversion of CO_2: An Organometallic Perspective, *Angew. Chem., Int. Ed.*, 2021, **60**, 11628–11686.
41 F. A. LeBlanc, A. Berkefeld, W. E. Piers and M. Parvez, Reactivity of Scandium β-Diketiminate Alkyl Complexes with Carbon Dioxide, *Organometallics*, 2012, **31**, 810–818.
42 W.-H. Wang, Y. Himeda, J. T. Muckerman, G. F. Manbeck and E. Fujita, CO_2 Hydrogenation to Formate and Methanol as an Alternative to Photo- and Electrochemical CO_2 Reduction, *Chem. Rev.*, 2015, **115**, 12936–12973.
43 D. W. Beh, W. E. Piers, I. del Rosal, L. Maron, B. S. Gelfand, C. Gendy and J.-B. Lin, Scandium alkyl and hydride complexes supported by a pentadentate diborate ligand: reactions with CO_2 and N_2O, *Dalton Trans.*, 2018, **47**, 13680–13688.
44 M.-M. Yang, D. J. Kim and M. Alexe, Flexo-photovoltaic effect, *Science*, 2018, **360**, 904–907.
45 Y. S. Zholdassov, L. Yuan, S. R. Garcia, R. W. Kwok, A. Boscoboinik, D. J. Valles, M. Marianski, A. Martini, R. W. Carpick and A. B. Braunschweig, Acceleration of Diels-Alder reactions by mechanical distortion, *Science*, 2023, **380**, 1053–1058.
46 P. Giannozzi, *et al.*, QUANTUM ESPRESSO: a modular and open-source software project for quantum simulations of materials, *J. Phys.: Condens. Matter*, 2009, **21**, 395502.
47 J. P. Perdew, K. Burke and M. Ernzerhof, Generalized Gradient Approximation Made Simple, *Phys. Rev. Lett.*, 1996, 77, 3865–3868.
48 K. F. Garrity, J. W. Bennett, K. M. Rabe and D. Vanderbilt, Pseudopotentials for highthroughput DFT calculations, *Comput. Mater. Sci.*, 2014, **81**, 446–452.
49 S. Grimme, J. Antony, S. Ehrlich and H. Krieg, A consistent and accurateab initioparametrization of density functional dispersion correction (DFT-D) for the 94 elements H-Pu, *J. Chem. Phys.*, 2010, **132**, 154104.
50 H. J. Monkhorst and J. D. Pack, Special points for Brillouin-zone integrations, *Phys. Rev. B*, 1976, **13**, 5188–5192.

